

First experimental proof of PET imaging based on multi-anode MCP-PMTs with Cherenkov radiator-integrated window

Weiyan Pan^{1,2,3,4}, Lingyue Chen^{1,2}, Guorui Huang⁵, Jun Hu^{1,2}, Wei Hou⁵, Xianchao Huang^{1,3,4}, Xiaorou Han^{1,3,4}, Xiaoshan Jiang^{1,2}, Zhen Jin⁵, Daowu Li^{1,3,4}, Jingwen Li⁵, Shulin Liu¹, Zehong Liang¹, Lishuang Ma¹, Zhe Ning^{1,2}, Sen Qian¹, Ling Ren⁵, Jianning Sun⁵, Shuguang Si⁵, Yunhua Sun^{1,2}, Long Wei^{1,2,3,4}, Ning Wang⁵, Qing Wei^{1,2,3,4}, Qi Wu^{1,2}, Tianyi Wang^{1,2,3,4}, Xin Wang^{1,2}, Xingchao Wang⁵, Yangfu Wang^{1,2,6}, Yifang Wang^{1,2}, Yingjie Wang^{1,2,4,5}, Zhi Wang⁵, Hang Yuan^{1,2,4,5}, Jingbo Ye^{1,2}, Xiongbo Yan^{1,2}, Meiling Zhu^{1,3,4}, Zhiming Zhang^{1,2,3,4}, On behalf of the MCP-PMT workgroup

¹ Institute of High Energy Physics, Chinese Academy of Sciences, Beijing 100049, China

² University of Chinese Academy of Sciences, Beijing 100049, China

³ Jinan Laboratory of Applied Nuclear Science, Jinan 250131, China

⁴ CAEA Centre of Excellence on Nuclear Technology Applications for Nuclear Detection and Imaging, Beijing, China

⁵ North Night Vision Science & Technology (Nanjing) Research Institute Co. Ltd, Nanjing 211100, China

E-mail: huangxc@ihep.ac.cn

Abstract

Improving the coincidence time resolution (CTR) of time-of-flight positron emission tomography (TOF-PET) systems to achieve a higher signal-to-noise ratio (SNR) gain or even direct positron emission imaging (dPEI) is of paramount importance for many advanced new clinical applications of PET imaging. This places higher demands on the timing performance of all aspects of PET systems. One effective approach is to use microchannel plate photomultiplier tubes (MCP-PMTs) for prompt Cherenkov photon detection. In this study, we developed a dual-module Cherenkov PET imaging experimental platform, utilising our proprietary 8 × 8-anode Cherenkov radiator-integrated window MCP-PMTs in combination with custom-designed multi-channel electronics, and designed a specific calibration and correction method for the platform. Using this platform, a CTR of 103 ps FWHM was achieved. We overcame the limitations of single-anode detectors in previous experiments, significantly enhanced imaging efficiency and achieved module-level Cherenkov PET imaging for the first time. Imaging experiments involving radioactive sources and phantoms of various shapes and types were conducted, which preliminarily validated the feasibility and advancement of this imaging method. In addition, the effects of normalisation correction and the interaction probability between the gamma rays and the MCP on the images and experimental results were analysed and verified.

Keywords: TOF-PET; Multi-anode MCP-PMT; Cherenkov radiation;

1. Introduction

Positron emission tomography (PET) is a valuable molecular imaging technology characterised by its unique functional imaging properties. It plays a crucial role in drug

research and disease diagnosis, particularly in the diagnosis of cancer (Boellaard *et al* 2015, Schwenck *et al* 2023) and various neurodegenerative diseases (Cavaliere *et al* 2020, Smith *et al* 2023). As clinical and research applications expand, new uses for PET have emerged. These include immuno-PET imaging (Lugat *et al* 2022), infectious disease imaging (Eibschutz *et al* 2022), and fetal imaging (Smith *et al* 2024), which require improved PET system sensitivity for faster and lower-dose imaging.

One of the principal factors influencing the signal-to-noise ratio (SNR) and image quality in a PET system is the time resolution (Karp *et al* 2008). Time-of-flight PET (TOF-PET) imaging incorporates TOF information into the reconstruction process. The utilisation of TOF information in conjunction with the time resolution of the system restricts the reconstructed locations of the annihilation point to a specific range, as opposed to the equal weighting of all locations along the entire line of response (LOR) as in traditional PET. This results in a gain in SNR and enhances the effective sensitivity of the PET system (Lecoq 2017). As a new imaging modality that can directly localise the annihilation position using TOF information without tomographic reconstruction, direct positron emission imaging (dPEI) brings greater performance enhancements to the PET system, enables more imaging methods and imaging algorithms (Onishi *et al* 2024), and puts higher demands on the fast-timing detector (Lecoq *et al* 2020).

Currently, the combination of lutetium-based scintillators and silicon photomultipliers (SiPMs) represents the prevailing detector scheme for PET systems (Gundacker *et al* 2020, Nadig *et al* 2023). The coincidence time resolution (CTR) of the most advanced PET systems has reached approximately 200 ps Full Width at Half Maximum (FWHM) (Van Sluis *et al* 2019, Prenosil *et al* 2022), with the best systems achieving 178 ps FWHM (Anon n.d.). At this level of coincidence time resolution, the benefits of TOF technology are already evident. However, there is still a gap to be bridged before truly effective dPEI (Ota *et al* 2019b) can be achieved or many of the advanced PET applications mentioned above can be realised. Therefore, further improvements are required in the timing performance of the PET detector.

To further improve the timing performance of PET detectors, it is imperative to minimise the time uncertainty derived from the photoelectric sensor throughout the photoelectric conversion and multiplication process. This necessitates a reduction in the single-photon time resolution (SPTR) (Gundacker *et al* 2023, 2019) or the single-photon transit time spread (TTS) (Bortfeldt *et al* 2020, Li *et al* 2020) of the photoelectric sensor. With regard to crystal luminescence, it is possible to develop scintillation crystals with a higher light yield and faster emission (Gundacker *et al* 2016, 2018). Furthermore, the constraints of the scintillation

luminescence process itself can be addressed by exploring alternative luminescence mechanisms. Consequently, another effective approach for improving the time resolution of PET detectors is to utilise faster luminescence mechanisms for detecting annihilation gamma rays. It is anticipated that this improvement will be significant (Korpar *et al* 2011). Cherenkov radiation is a phenomenon that occurs when a charged particle, such as an electron, travels through a dielectric medium at a speed exceeding the phase velocity of light in that medium (Kobzev 2010). Cherenkov photons are generated through electromagnetic polarisation and depolarisation of the medium, exhibiting a ‘prompt’ characteristic with rise and decay times of approximately 10 ps (Gundacker *et al* 2016). Therefore, the utilisation of Cherenkov light can serve to mitigate the time uncertainty that is inherent to the distribution of photons. This time uncertainty is relatively pronounced during the scintillation process. Consequently, Cherenkov photons can provide more precise timestamps than scintillation photons (Han *et al* 2021), and PET detection based on Cherenkov radiation is considered a promising way to achieve better CTR.

However, it is worth mentioning that the energy of the annihilation γ -rays is 511 keV, which results in a relatively low yield of Cherenkov photons (Kratochwil *et al* 2021). Furthermore, due to photon losses occurring during the transport and reception of light, Cherenkov detection in PET application often results in the detection of only a few photons or even a single photon. The microchannel plate photomultipliers (MCP-PMTs) employ a microchannel plate structure to replace the dynode in traditional PMTs, thereby achieving excellent timing performance and single-photon sensitivity. This is well aligned with the characteristics of Cherenkov photons, which are few in number and have fast responses, making it an optimal choice for high time resolution in Cherenkov PET detection.

The timing performance of the Cherenkov PET detection using MCP-PMT has been verified and reported. In one study, the Cherenkov radiator was used as the window material for the single-anode MCP-PMT (Ota *et al* 2019b). This choice aims to reduce the transmission loss of Cherenkov photons at the interface. In this study, a CTR of 26.4 ps FWHM was achieved, and direct imaging without reconstruction was achieved for the first time (Kwon *et al* 2021). However, because the MCP-PMT used in the study was single-anode, it lacked positional resolution. As a result, direct imaging must be achieved by collimated translational scanning. In addition, its sensitive area and overall shape prevent high-density multimodule assembly, making it difficult to meet the efficiency requirements of large PET systems. Therefore, the square multi-anode MCP-PMT is more suitable for PET applications due to its position-sensitive characteristics and ability to assemble multiple modules. Consequently, the square multi-anode MCP-PMT

has been the focus of some research (Ma *et al* 2023, Jones *et al* 2023) and serves as the detector solution used in this study.

In this work, we completed the experimental setup of a dual-module PET imaging platform using a pair of 8×8 -anode Cherenkov radiator-integrated window MCP-PMTs specifically designed and developed by our team. The readout and timing measurement of the MCP-PMT Cherenkov signals were accomplished using a multi-channel discriminator-based application specific integrated circuit (ASIC) chip, combined with a custom-designed multi-channel time-to-digital converter (TDC). Calibration and related corrections for each component of the platform were performed based on the characteristics of the multi-anode MCP-PMT and multi-channel electronics. A CTR test of the entire system was performed, resulting in a measured CTR of 103 ps FWHM. Imaging experiments were also carried out using point and rod sources, as well as a custom-designed ‘e⁺’ phantom with specific structures, achieving module-level Cherenkov PET imaging for the first time.

2. Materials

2.1 Multi-anode Cherenkov Radiator-integrated Window MCP-PMTs

In this work, we employed custom-designed multi-anode Cherenkov radiator-integrated window MCP-PMTs for annihilation gamma-ray detection based on the Cherenkov mechanism, as shown in Figure 1. The Cherenkov radiator-integrated window MCP-PMT uses lead glass as the window material, aiming to minimise light loss at the interface. The CTR and detection efficiency that can be achieved under different lead glass material thickness conditions are simulated using Geant4, as shown in Table 1.

Table 1. Simulation results of CTR and detection efficiency for different Cherenkov radiator thicknesses.

Single-photon TTS:	Thickness	2 mm	3 mm	4 mm	5 mm	7 mm
30 ps (σ)	CTR/ ps	88.68	91.12	93.15	94.53	100.20
	Detection efficiency	4.86%	6.93%	8.90%	10.53%	14.00%

Considering the detection efficiency, timing performance, and manufacturing process requirements, the window material thickness was determined to be 5.5 mm. The anodes of the MCP-PMT in the Cherenkov radiation detector are arranged in an 8×8 array with a pixel size of 5.5 mm \times 5.5 mm and a gap of 0.3 mm. The sensitive area of the entire multi-anode Cherenkov radiator-integrated window MCP-PMT is 46.1 mm \times 46.1 mm. Typical performance parameters of the multi-anode Cherenkov radiator-integrated window MCP-PMT were obtained by testing the central anode of the sample tube, as shown in Table 2.

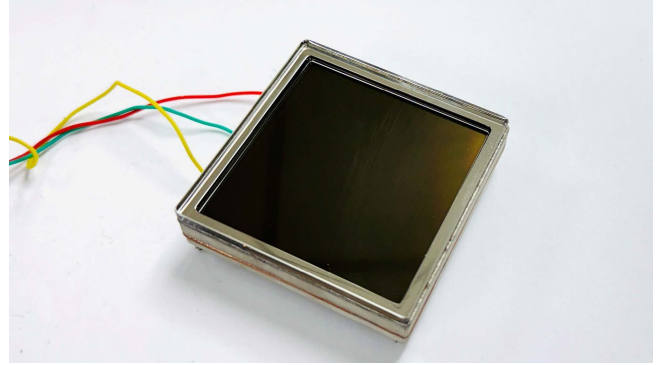


Figure 1. Photo of the multi-anode Cherenkov radiator-integrated window MCP-PMTs

TABLE 2. Typical performance parameters of multi-anode Cherenkov radiator-integrated window MCP-PMTs.

Detector	HV	Gain	Amplitude @SPE	Rise time	Fall time	TTS @SPE
MCP-PMT Sample 1	-1440 V	3.9E6	56.4 mV	296 ps	431 ps	27.4 ps(σ)
MCP-PMT Sample 2	-1485 V	4.4E6	52.4 mV	287 ps	479 ps	28.6 ps(σ)

2.2 Electronics

The Cherenkov signal output from the Cherenkov radiator-integrated window MCP-PMT has a relatively small amplitude and a much faster rise time of less than 300 ps. To address these characteristics of the Cherenkov signal, our team designed a multi-channel high-speed discriminator ASIC called FPMTread, as shown in Figure 2a. The FPMTread chip pre-amplifies the input signal through the receiver stage, compares it with the threshold, and amplifies the part of the signal that exceeds the threshold to saturation. It is then differentially output through the CML driver, and the width of the output signal is related to the over-threshold time of the original signal. The principle is shown in Figure 2b. The performance parameters of the chip are shown in Table 3, and it is also compared with other discriminator ASICs currently used in PET.

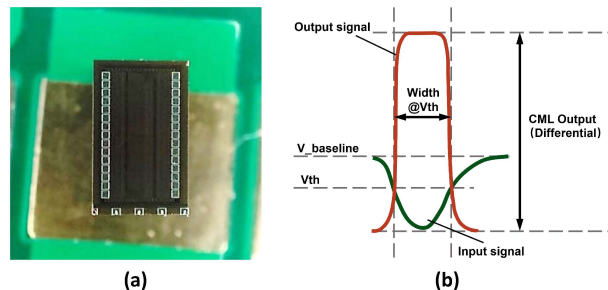


Figure 2. Photo of the FPMTread ASIC chip (a) and a schematic diagram of its principle (b).

TABLE 3. The main performance parameters of the FPMTread and comparison with mainstream multi-channel discriminator ASICs.

Organization	IHEP	CERN	University of Barcelona
ASIC	FPMTread	NINO	HRflexTOT
Technology	0.13- μm CMOS	0.25- μm CMOS	0.18- μm CMOS
Bandwidth	2GHz	500MHz	500MHz
Number of channels	4	8	16
Time jitter(rms)	4.62 ps	<25ps	\sim 7ps

An FPGA-based TDC is used as the digital electronics to implement the measurement of time information. The board has 64 TDC channels, with every two channels forming a group responsible for detecting the time information of the rising and falling edges of a signal to achieve the measurement of the pulse width. Each TDC board can realise the time measurement of 32 detector channels. The TDC has a measured precision of less than 6 ps RMS and is capable of achieving multi-module synchronous measurement.

In order to meet the integration requirements for multi-channel measurements and to reduce the performance loss due to signal transfer and transmission, we combined the discriminator ASIC readout circuits and the FPGA-based TDC circuits into one electronic board. Each electronic board contains eight 4-channel FPMTread discriminator ASICs and one 32-channel FPGA-based TDC circuit. Independent threshold adjustment of each discriminator channel is also implemented by the FPGA in combination with multi-channel digital-to-analogue converter (DAC) chips. Differential clock ports for receiving synchronous clocks and an RST port for receiving reference signals have also been added for multi-module time synchronisation. Based on the test method shown in Figure 3a, the electronic board measured a timing precision of 10.34 ps (σ) under the condition of multi-module synchronisation. The measurement results are shown in Figure 3b.

2.3 Detector Modules

To integrate the electronics and the Cherenkov radiator-integrated window MCP-PMT into a detector module, a readout board was designed to transmit the signals from the 64 anodes using coaxial connectors. To ensure the quality and integrity of the signal transmission, the signals are fed into the electronics board via a 10 cm coaxial cable. A metal structure was designed to support and connect the electronics boards to the Cherenkov radiator-integrated window MCP-PMT, allowing effective heat dissipation. The complete detector module is shown in Figure 3c. Each module consists of an 8×8 anode Cherenkov radiator-integrated window MCP-PMT and two 32-channel electronics boards.

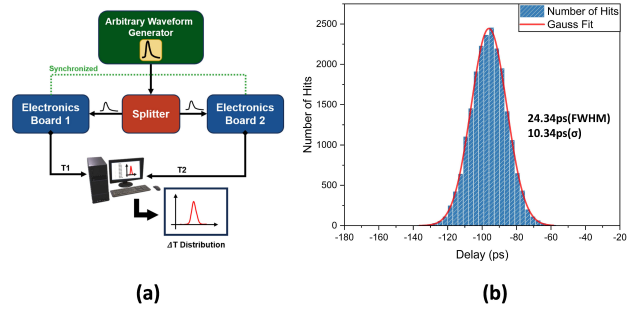


Figure 3. Schematic diagram of the method for the timing performance test of electronics (a) and the test results (b). Detector module based on Cherenkov radiator-integrated window MCP-PMT (c).

3. Methods

3.1 Experimental Setup of Dual-module PET Imaging Platform

Figure 4 shows the experimental setup for a dual-module PET imaging platform based on Cherenkov radiator-integrated window MCP-PMTs. Two detector modules were arranged face to face at a distance of 46.1 mm, corresponding to the side length of the detector sensitivity region. The radioactive source or imaging object used in the experiment was placed in the centre of the field of view (FOV) and was equipped with a rotary stage for multi-angle acquisition. After calibrating the voltage-count rate curve, the voltages of the two MCP-PMTs were set to -1500 V and -1550 V (V6534 HV power supply module, CAEN). A commercial clock board (Si5361-EB, Skyworks) and a custom-designed RST board form a clock and synchronisation module. The commercial clock board supplies synchronised clocks to multiple modules. The RST board supplies reference signals with fixed time differences to all modules based on the synchronised clock. This signal clears the coarse time of the TDC, achieving time synchronisation across multiple modules. The measured time information is transmitted directly to the host computer via the Gigabit Ethernet port for real-time acquisition and processing.

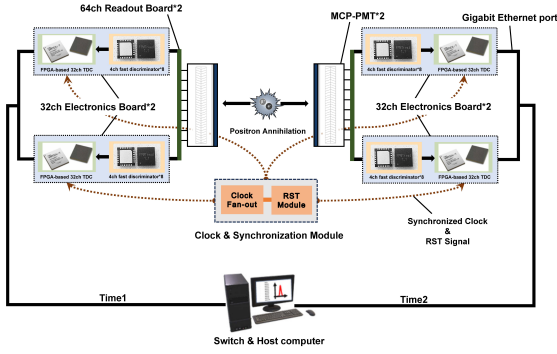


Figure 4. Schematic diagram of the dual-module Cherenkov PET imaging platform structure and components.

3.2 Preparation of Experiment

After setting up the experiment, a series of calibrations and corrections are required to ensure consistency among the multiple channels of the detector module before conducting the experiment. The preparatory work for this experiment is as follows:

3.2.1 Baseline Calibration and Threshold Setting.

As described above, in the working principle of the FPMTread discriminator ASIC chip, the input signal of the discriminator is added to a baseline. The threshold value needs to be set with reference to this baseline. However, due to process variations in chip manufacturing, the baseline of each channel varies. To accurately set the threshold value, it is necessary to calibrate the baseline of each channel individually. We performed a threshold scan with an accuracy of 1 mV and recorded the value when the noise triggered as the channel baseline to obtain channel-by-channel baseline calibration data. The results are shown in Figure 5a and are used as references for subsequent threshold setting.

Referring to the previous results of the performance test of the sample Cherenkov radiator-integrated window MCP-PMTs (Ma *et al* 2023), the gain of different anodes of the Cherenkov radiator-integrated window MCP-PMTs varies and shows a geometrical pattern, with high gain in the centre and low gain at the edge. The difference between the edge and the centre is approximately 1.7 times. Based on this characteristic, we set the threshold "by ring", as shown in Figure 5b. The single-photon amplitude distribution of the centre anode of the MCP-PMTs has a peak level of about 50 mV. Based on the timing threshold of a quarter of the single-photon amplitude, we set the thresholds from the centre to the edge at 13 mV, 11 mV, 9 mV, and 7 mV, respectively.

3.2.2 Detection Efficiency Uniformity Calibration. To establish normalisation correction parameters for the CASToR reconstruction and to verify the validity of the threshold-setting method and baseline calibration, we

performed uniformity calibrations of the detection efficiency both before and after the baseline calibration and the "by ring" threshold setting. We used a ^{137}Cs point source, as shown in Figure 5c, positioned approximately 300 mm from the detector to minimise counting differences between anodes due to solid angle variations. After placing the radioactive source, we evaluated the count rates of the different anodes and subtracted the pre-measured dark count rate to determine changes in the detector count rate response, which served as a reference for uniformity calibration. As shown in Figure 5d, after normalising the data, the standard deviation of the uniformity calibration results for the same detector decreased from 0.323 before baseline calibration and the "by ring" threshold-setting method to 0.190 afterwards. This indicates that the uniformity between detector channels was significantly improved after the channel-by-channel baseline calibration and the "by ring" threshold-setting method. Based on these optimised results, we obtained normalisation correction parameters for each LOR, which were used for subsequent image reconstruction.

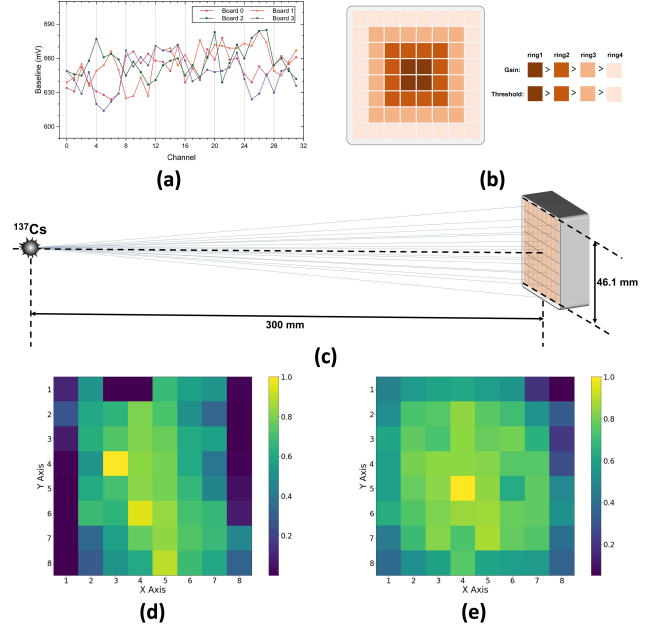


Figure 5. Baseline calibration results (a) and a schematic diagram of the "by ring" threshold-setting method (b). Schematic diagram of the experimental setup for the detection efficiency uniformity calibration (c). Results of detection efficiency uniformity before (d) and after (e) the baseline calibration and the application of the "by ring" threshold-setting method.

3.2.3 Time Correction.

In multi-channel time measurement experiments like this study, some fixed time delays between channels are unavoidable due to differences in signalling distances and the length of the delay chain within the FPGA. To improve time resolution and mitigate the effects of these fixed time delays, channel-by-channel timing calibration is essential. As shown in Figure 6a, we placed two detectors 30 mm apart and

positioned a ^{22}Na point source adjacent to one of the detectors. We utilised the nearest anode as the reference channel and the 64 channels of the other detector as the channels to be corrected. As illustrated in Figure 6b, this setup allowed us to obtain the distribution of time differences of coincident events between each detector channel and the reference channel. We then determined the peak positions and calculated the theoretical peak positions for each time distribution based on the optical path differences of the gamma photon pairs. Corrections were calculated for each channel based on the differences between these two values.

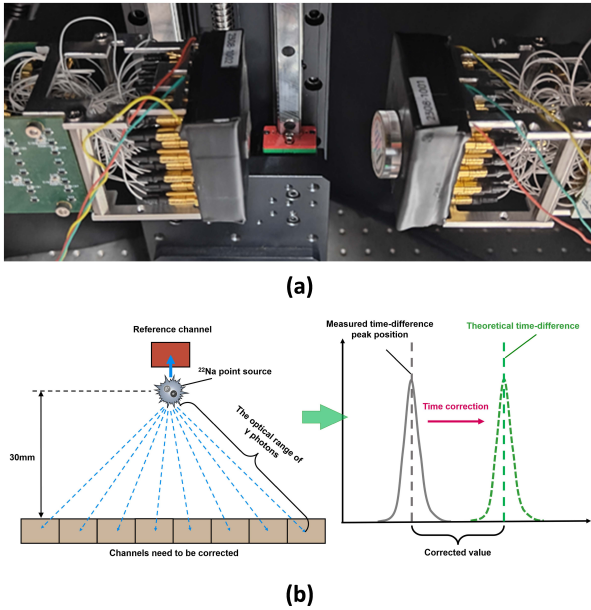


Figure 6. Experimental setup (a) and schematic diagram (b) of time correction.

We applied the aforementioned method to perform time corrections for each channel. Before and after the correction, we selected a fixed reference channel and recorded the coincidence events between it and the 64 anodes of the other detector. We measured the peak positions of the coincidence time distributions for the 64 LORs. The results are shown in Figure 7. After the correction, the peak positions of the coincidence time distributions for all LORs are close to 0 ps. This aligns with the position of the point source in the experiment, which is exactly in centre of the field of view, thus confirming the reliability of the time correction.

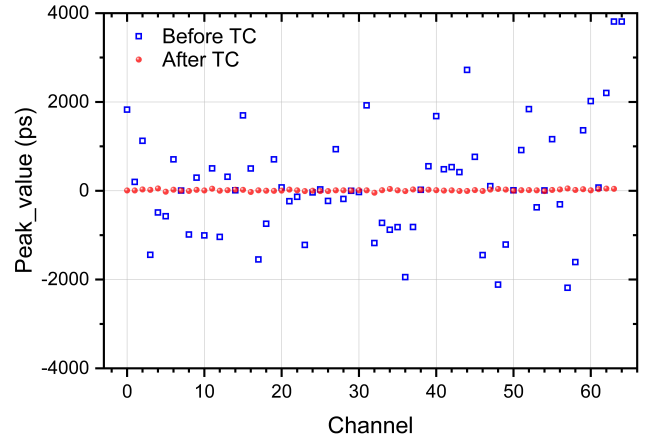


Figure 7. Peak positions of time distributions before and after time correction on the sample LORs

3.3 Acquisition Method, Image Reconstruction and Correction

As shown in Figure 8, the distance between two detector modules was set to be equal to the sensitive area of the detector (i.e., 46.1 mm), and the object to be imaged was placed at the centre of the field of view and rotated once through 90° during the experiment to achieve comprehensive data acquisition from all four sides.

Image reconstruction and associated data corrections were performed using the CASToR software toolkit. The detectors were configured in CASToR according to the same setup described in the previous section on the acquisition method. The system matrix was generated, and the detection efficiency calibration results were organised on a line-by-line basis according to the requirements of the normalisation correction file. Finally, the detector performance parameters were set based on the results of the performance tests conducted in advance.

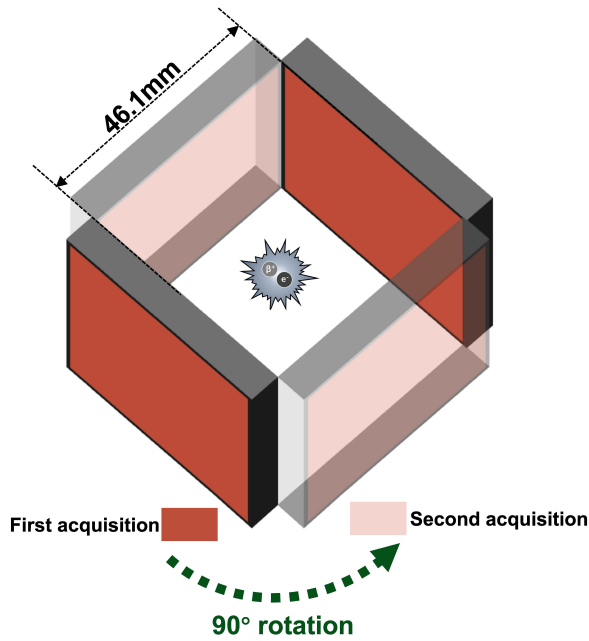


Figure 8. Schematic diagram of the image acquisition method and the arrangement of detectors in CASToR

4. Results

4.1 Point and Rod Source PET Imaging

After all corrections and calibrations were completed, imaging experiments with point and rod sources were conducted according to the layout described in the previous acquisition method, as shown in Figure 9a. The radioactive source in the point source experiment was ^{22}Na , with a diameter of 0.25 mm and an activity of approximately 27 μCi , while the radioactive source in the rod source experiment was ^{68}Ge , with a diameter of 2.36 mm, a length of 256 mm, and an activity of approximately 10 μCi .

As shown in Figure 9b, the system successfully achieved Cherenkov PET imaging and reconstruction of a point source. In the imaging results, a straight line in the x-direction passing through the centre of the point source image was plotted, and a Gaussian fit was applied to the distribution of pixel values along its path to evaluate the image resolution capability of the two-module system. The fitting result yielded a FWHM of 3.05 mm, which is consistent with the results of the simulation. These experimental results provide preliminary verification of the feasibility of achieving Cherenkov PET imaging based on the integrated-window multi-anode MCP-PMT.

After completing the point-source imaging experiments, rod-source imaging experiments were performed both before and after applying the normalisation correction, with the experimental results shown in Figure 9c. The reconstructed images without normalisation correction exhibited noticeable missing areas at both ends, which were filled in after

applying the normalisation correction. full-field imaging was achieved with a dual-module Cherenkov PET system, and the results of the rod-source imaging verified the validity of the normalisation correction while illustrating the importance of uniformity between the pixels of the detector modules.

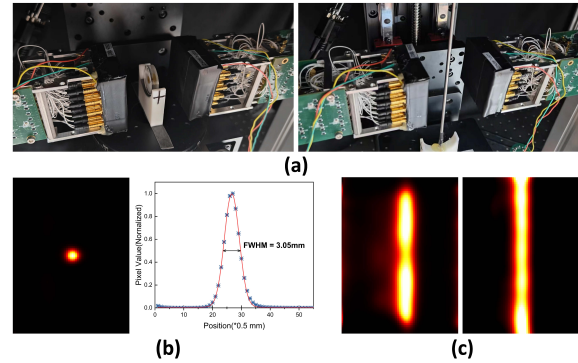


Figure 9. Point source, rod source imaging experiments (a) and point source image results and analysis (b), rod source image before and after normalisation correction (c).

4.2 CTR Test

The coincidence time resolution of the platform was analysed based on data from the point source imaging experiments. All data on the lines of LORs with a certain level of coincidence counts were summarised to obtain an overall time distribution for the platform, as shown in Figure 10. In this version of the integrated-window multi-anode MCP-PMT, although a solution has been identified during the process and will be implemented in subsequent prototypes, the microchannel plate (MCP) material currently used still contains a certain amount of lead. Therefore, the microchannel plate and the annihilation gamma rays also have a certain cross section of interaction, based on the coincidence events in which the two gamma rays interact with the MCP-PMT. Specifically, these are categorised as follows: radiator optical window-radiator optical window, MCP (left)-radiator optical window, radiator optical window-MCP (right), and others (includes photo-electron backscatter and MCP-MCP interactions, etc.) (Ota *et al* 2020a). The coincidence events are divided into four categories, and a 4-Gaussian fit to the total time distribution was performed (see Figure 10), with the specific parameters of each Gaussian peak shown in Table 4.

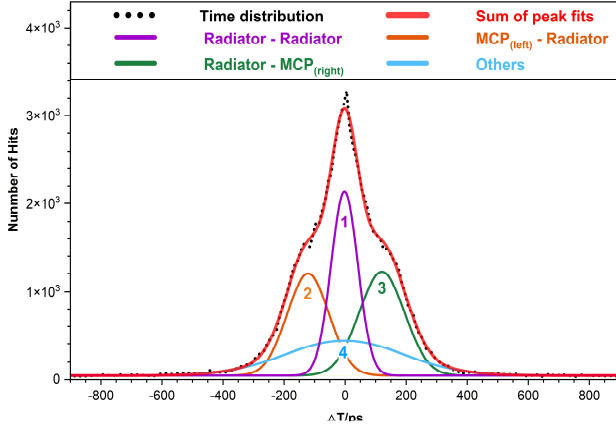


Figure 10. Time distribution decomposed by four categories of coincidence event.

TABLE 4. Fitting parameters for a four-Gaussian fit.

Peak number	Type of interaction	A	Xc	FWHM	Event ratio
1	Radiator - Radiator	229025.1 5	-1.97 ps	103.17 ps	27.32 %
2	MCP _(left) - Radiator	198512.4 6	-121.19 ps	161.60 ps	22.75 %
3	Radiator - MCP _(right)	220051.8 5	120.46 ps	176.12 ps	26.25 %
4	Others	190644.8 4	-1.96 ps	458.79 ps	22.68 %

In Figure 10 and Table 4, the four peaks numbered 1 to 4 correspond to the coincidence events under the four interaction modes described above. It is important to note that in the current MCP-PMT design, the distance between the photocathode and the MCP is 0.4 mm, with a voltage of ~ 130 V applied across them. According to the formula for calculating the drift time of photoelectrons in the electric field between the cathode and the MCP, the corresponding electron drift time is approximately 118 ps. The peak differences between the two side peaks and the main peak are 121 ps and 120 ps, respectively, which corresponds to the electron drift time. This further confirms that the cause of the side peaks is indeed the annihilation gamma rays interacting with the MCP material. This problem will be addressed by eliminating the lead in the MCP material and further optimising the blocking capability and detection efficiency of the optical window material. The main peak numbered 1 has a 103 ps FWHM. This represents the level of time resolution obtained without any data filtering or correction. This serves as an initial demonstration of the advantages and potential of Cherenkov PET imaging and the integrated-window MCP-PMT in improving time resolution.

4.3 e^+ Phantom Imaging

In addition, we demonstrated the Cherenkov PET imaging results of the platform for structured objects. Considering the size of the dual module and the experimental setup, we specifically designed the e^+ shaped phantom. The design of

the phantom and the picture of the experiment are shown in Figure 11a and Figure 11b, with a side length of 35 mm and a tube diameter of 1.5 mm.

The imaging result of the e^+ module is shown in Figure 11c. To the best of our knowledge, this is the first study to achieve module-level PET imaging based on the Cherenkov mechanism. This verifies the feasibility of Cherenkov imaging at a certain scale. Although there is still some degree of non-uniformity between the channels, resulting in highlights at the corners of the phantom and unclear representation at the “+” region, overall, it clearly reflects the majority of the structural information of the e^+ phantom, and these issues will be addressed in subsequent efforts to optimise homogeneity and apply better normalisation corrections.

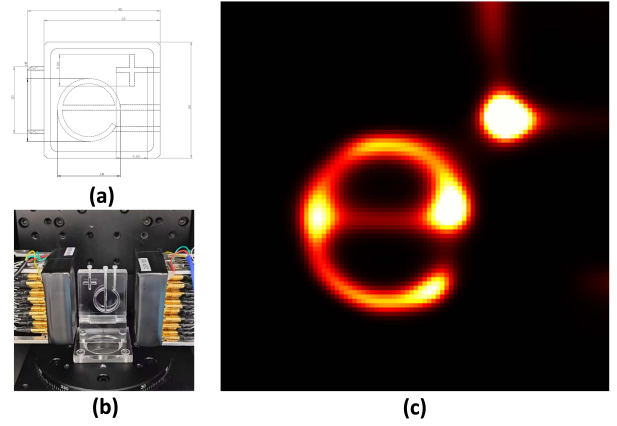


Figure 11. Phantom design (a) and experimental setup (b) and Experimental result of e^+ phantom imaging (c)

5. Discussion

In this study, we developed a dual-module PET imaging platform utilising a multi-anode MCP-PMT with an integrated window of Cherenkov radiators, performed specialised calibrations and corrections to account for the unique characteristics of the platform, evaluated its timing performance, and conducted preliminary imaging experiments.

Prior to this study, Cherenkov-based PET imaging research had been conducted using single-pixel devices. In recent research, an excellent time resolution was achieved, and direct imaging was accomplished using a single-anode MCP-PMT with integrated window material (Kwon *et al* 2021). However, because the single-anode MCP-PMT lacks positional resolution capability, the localisation of the radiation source is accomplished through collimation and translation of the detector, which significantly impacts imaging efficiency. This represents the most significant obstacle to the practical implementation of this modality in PET. Our self-developed multi-anode MCP-PMT not only

increases the sensitive area but also enables multi-module assembly while reducing the minimising the percentage of the dead zone. Furthermore, the multi-anode design endows the detector with positional resolution capabilities, eliminating the need for collimation and translation, which are primary contributors to the low efficiency.

As mentioned above, in our imaging experiments, the activity of the radioactive source and the imaging time required for imaging a similar phantom were reduced from >2 mCi and 24 hours in previous single-anode MCP-PMT experiments to <200 μ Ci and approximately 30 minutes, representing a significant improvement in efficiency. Moreover, by utilising custom-designed multi-channel high-precision electronics instead of a high-precision oscilloscope, power consumption is reduced, and the limitations regarding channel count are overcome while maintaining measurement accuracy, thereby improving the efficiency of time measurement, data acquisition and processing, making it more feasible for practical applications.

However, because the time resolution of the multi-anode MCP-PMT remains inferior to that of the single-anode MCP-PMT and the complexity of the correction work significantly increases with the number of anodes, direct imaging under multi-anode MCP-PMT conditions has yet to be achieved. In fact, by employing the pulse-cutting analysis signal screening method (Ota *et al* 2021), it has been verified that the current multi-anode sample tube can achieve a time resolution of approximately 40 ps FWHM using this approach (Chen *et al* 2024). Although most instances were screened out, this method can still be used to initially validate the imaging performance and image quality of the direct imaging mode under position-sensitive conditions. This will be our next focus. Additionally, efforts will continue to enhance the timing performance of the detector. It is anticipated that the demand for a direct imaging mode without data filtering will be fulfilled, and the resulting performance improvement of the PET system will be extraordinary. Besides the potential for realising a new imaging method (Onishi *et al* 2024), precise time information can help eliminate scattered events more effectively, which significantly compensates for the limitations of the Cherenkov mechanism in providing effective energy information. This is also a key discussion point regarding this imaging modality.

It is important to note that, although Cherenkov imaging at the module level has been achieved, the uniformity of the system in current experiments remains suboptimal. This is largely attributed to the unique characteristics of the Cherenkov mechanism. Due to the energy of the annihilated gamma rays, the detection of Cherenkov light often occurs at the level of a few photons or even at the single-photon level. Consequently, the gamma-ray signal cannot be distinguished from the dark noise of the detector itself. If the dark noise

level is high or unstable, it will directly impact the calibration and correction results of the detector. Additionally, the relatively weak signal exacerbates the effects of gain variations among detector pixels and response differences between electronic channels. As noted earlier, the uniformity of the system has been initially addressed through complex calibration and specialised threshold-setting methods; however, normalisation correction remains necessary, and the quality of the image is highly dependent on the reliability of this normalisation correction. Therefore, subsequent work will also focus on enhancing the consistency of the detector itself, while simultaneously exploring more reliable calibration and normalisation correction methods to minimise the impact of non-uniformity on imaging.

By analysing the system's total coincidence time distribution, the time resolution of the main peak event is approximately 103 ps FWHM. Based on simulations, under the current conditions of the sample tube, more than 60% of the detected annihilated gamma photons result in the production of one photoelectron. Referring to the current single-photon TTS of the sample tube, the coincidence time resolution obtained under the detector-only condition is approximately 94 ps FWHM. By combining the previously measured timing precision of the electronics at 24.3 ps FWHM, it is estimated that the coincidence time resolution of the system is approximately 97 ps FWHM. The experimental results align with the theoretical calculations. The discrepancy of a few ps may arise from variations in peak position accuracy resulting from a lack of statistics in some channels during multi-channel time correction.

In the time distribution results, there are annoying side peaks symmetrically located on both sides of the main peak. After analysing the experimental results and referencing previous studies (Ota *et al* 2019a, 2020b), it was determined that the source of the side peaks is the interaction between the annihilation gamma rays and the MCP. The presence of such peaks not only affects the overall time resolution and efficiency, as seen in single-anode applications, but also directly affects the spatial resolution in position-sensitive detector applications. As shown in Figure 12, this directly shifts the positioning of the annihilation point. Therefore, it is crucial to suppress this aspect of the events as much as possible. Reducing or even eliminating the lead content in the MCP is the most direct approach to suppressing the interaction between radiation and the MCP. The efficacy of this approach has been confirmed in previous studies, and we are currently optimising it for this purpose, which will be implemented in the next version of the sample tube. Furthermore, the lead glass currently in use is not the optimal material for integrating windows for Cherenkov radiation. The use of lead glass at present is primarily related to the challenges associated with the relevant processing techniques.

A comprehensive consideration of core factors such as density, refractive index, and cutoff wavelength indicates that more suitable alternatives, such as HfO_2 or PbF_2 , exist. By optimising the light window material, the number of Cherenkov photons produced by the annihilation of gamma rays will also increase, subsequently leading to an increase in the number of photoelectrons. According to the principle that the timing response of the detector is proportional to $1/n$, the time resolution will be significantly improved. Simultaneously, the new light window material will enhance detection efficiency, further suppressing the impact of the interaction between the gamma rays and the MCP, while also improving imaging efficiency. In fact, we have conducted research on the processing techniques and technologies of alternative light window materials. However, some challenges remain. It is anticipated that, in the near future, prototype tubes utilising superior materials as Cherenkov integrated windows will be successfully developed.

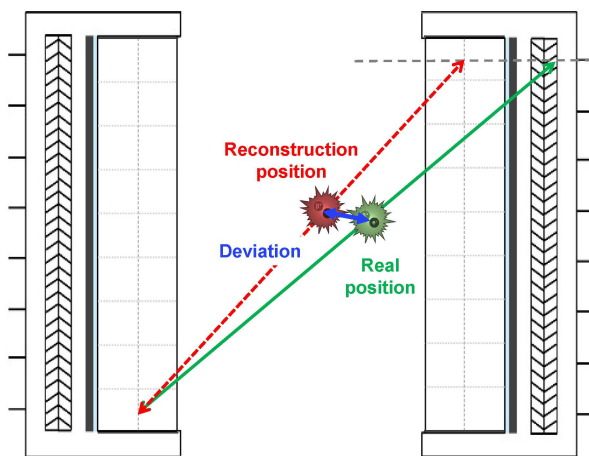


Figure 12. Illustration of the positioning error caused by the interaction between the annihilation gamma rays and the MCP.

In summary, we have developed a dual-module PET imaging platform based on a multi-anode integrated window MCP-PMT, which has been tested to achieve a CTR of 103 ps FWHM for the main peak and has successfully demonstrated Cherenkov PET imaging at the module level for the first time. However, as discussed previously, several challenges remain to be addressed, including system uniformity, the interaction of radiation with the MCP, and the need for further improvements in imaging efficiency. Nonetheless, effective strategies exist to address these challenges. Our research has elevated the scale of Cherenkov PET imaging, and the experimental results have confirmed the significant potential of this model for further enhancing imaging performance and quality.

6. Conclusion

In this study, we developed the first dual-module module-level PET imaging experimental platform, utilising our self-

developed multi-anode Cherenkov radiator-integrated window MCP-PMTs combined with custom-designed multi-channel electronics, and designed a special calibration and correction method for the platform. Based on the platform, we achieved the first module-level Cherenkov PET imaging for various shapes of radioactive sources and phantoms, overcoming the limitations of single-anode detectors in previous experiments and significantly improving imaging efficiency. Additionally, the entire platform demonstrated a CTR of 103 ps FWHM, initially verifying the feasibility and advancement of this imaging modality. Furthermore, we analysed and verified the effects of normalisation correction and the interaction probability between the gamma rays and the MCP on the images and experimental results.

Acknowledgements

This work was supported in part by the National Natural Science Foundation of China (Grant Nos. 12075267, 12275291, 12175265, 12205117) and Research Instrument and Equipment Development Project of Chinese Academy of Sciences (Grant No. YJKYYQ20200015)

References

- Anon Siemens Healthineers Debuts Biograph Vision.X PET/CT Scanner Online: <https://www.siemens-healthineers.com/en-us/press-room/press-releases/biograph-vision-x-pet-ct-scanner-debut>
- Boellaard R, Delgado-Bolton R, Oyen W J G, Giammarile F, Tatsch K, Eschner W, Verzijlbergen F J, Barrington S F, Pike L C, Weber W A, Stroobants S, Delbeke D, Donohoe K J, Holbrook S, Graham M M, Testanera G, Hoekstra O S, Zijlstra J, Visser E, Hoekstra C J, Pruim J, Willemsen A, Arends B, Kotzerke J, Bockisch A, Beyer T, Chiti A and Krause B J 2015 FDG PET/CT: EANM procedure guidelines for tumour imaging: version 2.0 *Eur. J. Nucl. Med. Mol. Imaging* **42** 328–54
- Bortfeldt J, Brunbauer F, David C, Desforge D, Fanourakis G, Gallinaro M, García F, Giomataris I, Gustavsson T, Guyot C, Iguaz F J, Kebbiri M, Kordas K, Legou P, Liu J, Lupberger M, Manthos I, Müller H, Niaouris V, Oliveri E, Papaevangelou T, Paraschou K, Pomorski M, Resnati F, Ropelewski L, Sampsonidis D, Schneider T, Schwemling P, Scorsone E, Sohl L, van Stenis M, Thuiner P, Tsiolitis Y, Tzamaris S E, Veenhof R, Wang X, White S, Zhang Z and Zhou Y 2020 Timing performance of a Micro-Channel-Plate Photomultiplier Tube *Nucl. Instruments Methods Phys. Res. Sect. A Accel. Spectrometers, Detect. Assoc. Equip.* **960** 163592 Online: <https://doi.org/10.1016/j.nima.2020.163592>
- Cavaliere C, Tramontano L, Fiorenza D, Alfano V, Aiello M and Salvatore M 2020 Gliosis and Neurodegenerative Diseases: The Role of PET and MR Imaging *Front. Cell. Neurosci.* **14** 1–13
- Chen L, Ma L, Huang G, Hua Z, Jin M, Jin Z, Qian S, Ren L, Si S, Sun J, Wu Q, Wang X, Wang Y, Wang Z, Wang N, Wu K and Zhang H 2024 Coincidence time resolution of 50 ps FWHM using a pair of multi-anode MCP-PMTs with Cherenkov radiator window *Nucl. Instruments Methods Phys. Res. Sect. A Accel. Spectrometers, Detect. Assoc. Equip.*

- Eibschutz L S, Rabiee B, Asadollahi S, Gupta A, Assadi M, Alavi A and Gholamrezanezhad A 2022 FDG-PET/CT of COVID-19 and Other Lung Infections *Semin. Nucl. Med.* **52** 61–70 Online: <https://doi.org/10.1053/j.semnuclmed.2021.06.017>
- Gundacker S, Auffray E, Pauwels K and Lecoq P 2016 Measurement of intrinsic rise times for various L(Y)SO and LuAG scintillators with a general study of prompt photons to achieve 10 ps in TOF-PET *Phys. Med. Biol.* **61** 2802–37
- Gundacker S, Borghi G, Cherry S R, Gola A, Lee D, Merzi S, Penna M, Schulz V and Kwon S II 2023 On timing-optimized SiPMs for Cherenkov detection to boost low cost time-of-flight PET *Phys. Med. Biol.* **68**
- Gundacker S, Martinez Turtos R, Kratochwil N, Pots R H, Paganoni M, Lecoq P and Auffray E 2020 Experimental time resolution limits of modern SiPMs and TOF-PET detectors exploring different scintillators and Cherenkov emission *Phys. Med. Biol.* **65** ab63b4 Online: <https://doi.org/10.1088/1361-6560/ab63b4>
- Gundacker S, Turtos R M, Auffray E and Lecoq P 2018 Precise rise and decay time measurements of inorganic scintillators by means of X-ray and 511 keV excitation *Nucl. Instruments Methods Phys. Res. Sect. A Accel. Spectrometers, Detect. Assoc. Equip.* **891** 42–52 Online: <https://doi.org/10.1016/j.nima.2018.02.074>
- Gundacker S, Turtos R M, Auffray E, Paganoni M and Lecoq P 2019 High-frequency SiPM readout advances measured coincidence time resolution limits in TOF-PET *Phys. Med. Biol.* **64**
- Han X, Wei L, Huang X, Tang H, Wang Y, He W, Li D and Zhang Z 2021 Simulation research on time resolution based on Cherenkov radiation *Radiat. Detect. Technol. Methods* **5** 421–9 Online: <https://doi.org/10.1007/s41605-021-00266-5>
- Jones T, Bhasin S, Blake T, Brook N H, Cicala M F, Conneely T, Cussans D, van Dijk M W U, Forty R, Frei C, Gabriel E P M, Gao R, Gershon T, Gys T, Hadavizadeh T, Hancock T H, Harnew N, Kreps M, Milnes J, Piedigrossi D, Rademacker J and Smallwood J C 2023 New developments from the TORCH R&D project *Nucl. Instruments Methods Phys. Res. Sect. A Accel. Spectrometers, Detect. Assoc. Equip.* **1045** 167535 Online: <https://doi.org/10.1016/j.nima.2022.167535>
- Karp J S, Surti S, Daube-Witherspoon M E and Muehlethner G 2008 Benefit of time-of-flight in PET: Experimental and clinical results *J. Nucl. Med.* **49** 462–70
- Kobzev A P 2010 The mechanism of Vavilov-Cherenkov radiation *Phys. Part. Nucl.* **41** 452–70
- Korpar S, Dolenc R, Križan P, Pestotnik R and Stanovnik A 2011 Study of TOF PET using Cherenkov light *Nucl. Instruments Methods Phys. Res. Sect. A Accel. Spectrometers, Detect. Assoc. Equip.* **654** 532–8
- Kratochwil N, Gundacker S and Auffray E 2021 A roadmap for sole Cherenkov radiators with SiPMs in TOF-PET *Phys. Med. Biol.* **66**
- Kwon S II, Ota R, Berg E, Hashimoto F, Nakajima K, Ogawa I, Tamagawa Y, Omura T, Hasegawa T and Cherry S R 2021 Ultrafast timing enables reconstruction-free positron emission imaging *Nat. Photonics* **15** 914–8
- Lecoq P 2017 Pushing the Limits in Time-of-Flight PET Imaging *IEEE Trans. Radiat. Plasma Med. Sci.* **1** 473–85
- Lecoq P, Morel C, Prior J O, Visvikis D, Gundacker S, Auffray E, Križan P, Turtos R M, Thers D, Charbon E, Varela J, De La Taille C, Rivetti A, Breton D, Pratte J F, Nuyts J, Surti S, Vandenberghe S, Marsden P, Parodi K, Benlloch J M and Benoit M 2020 Roadmap toward the 10 ps time-of-flight PET challenge *Phys. Med. Biol.* **65**
- Li Z, Li X, Cao Q, Li C, Wang Y, Liu J, Shao M, Peng H, Wang X, Zhou Y and Zhao Z 2020 Test and simulation of a Cherenkov picosecond timing counter *Nucl. Instruments Methods Phys. Res. Sect. A Accel. Spectrometers, Detect. Assoc. Equip.* **966** 163838 Online: <https://doi.org/10.1016/j.nima.2020.163838>
- Lugat A, Bailly C, Chérel M, Rousseau C, Kraeber-Bodéré F, Bodet-Milin C and Bourgeois M 2022 Immuno-PET: Design options and clinical proof-of-concept *Front. Med.* **9**
- Ma L, Chen L, Chai P, Liang Z, Huang G, Hu J, Han X, Hua Z, Huang X C, Jin M, Jiang X, Jin Z, Liu S, Pan W, Qian S, Ren L, Si S, Sun J, Wei L, Wu Q, Wang T, Wang X, Wang Y, Wang Y, Wang Z, Wang Z, Wang N, Wu K, Yan X, Zhang H and Zhang Z 2023 A novel multi-anode MCP-PMT with Cherenkov radiator window *Nucl. Instruments Methods Phys. Res. Sect. A Accel. Spectrometers, Detect. Assoc. Equip.* **1049**
- Nadig V, Herweg K, Chou M M C, Lin J W C, Chin E, Li C, Schulz V and Gundacker S 2023 Timing advances of commercial divalent-ion co-doped LYSO:Ce and SiPMs in sub-100 ps time-of-flight positron emission tomography *Phys. Med. Biol.* **68** 075002 Online: <https://iopscience.iop.org/article/10.1088/1361-6560/acbde4>
- Onishi Y, Hashimoto F, Ote K and Ota R 2024 Whole Reconstruction-Free System Design for Direct Positron Emission Imaging From Image Generation to Attenuation Correction *IEEE Trans. Med. Imaging* **43** 1654–63
- Ota R, Nakajima K, Hasegawa T, Ogawa I and Tamagawa Y 2019a Timing-performance evaluation of Cherenkov-based radiation detectors *Nucl. Instruments Methods Phys. Res. Sect. A Accel. Spectrometers, Detect. Assoc. Equip.* **923** 1–4
- Ota R, Nakajima K, Ogawa I, Tamagawa Y, Kwon S I, Berg E, Cherry S R, Shimoi H, Hasegawa Y, Nishizawa H, Shimano K and Hasegawa T 2021 Lead-free MCP to improve coincidence time resolution and reduce MCP direct interactions *Phys. Med. Biol.* **66**
- Ota R, Nakajima K, Ogawa I, Tamagawa Y, Shimoi H, Suyama M and Hasegawa T 2019b Coincidence time resolution of 30 ps FWHM using a pair of Cherenkov-radiator-integrated MCP-PMTs *Phys. Med. Biol.* **64**
- Ota R, Nakajima K, Ogawa I, Tamagawa Y, Shimoi H, Suyama M and Hasegawa T 2020a Precise analysis of the timing performance of Cherenkov-radiator-integrated MCP-PMTs: analytical deconvolution of MCP direct interactions *Phys. Med. Biol.* **65** 10NT03 Online: <https://iopscience.iop.org/article/10.1088/1361-6560/ab8c8f>
- Ota R, Nakajima K, Ogawa I, Tamagawa Y, Shimoi H, Suyama M and Hasegawa T 2020b Precise analysis of the timing performance of Cherenkov-radiator-integrated MCP-PMTs: Analytical deconvolution of MCP direct interactions *Phys. Med. Biol.* **65**
- Prenosil G A, Sari H, Fürstner M, Afshar-Oromieh A, Shi K, Rominger A and Hentschel M 2022 Performance Characteristics of the Biograph Vision Quadra PET/CT System with a Long Axial Field of View Using the NEMA NU 2-2018 Standard *J. Nucl. Med.* **63** 476–84
- Schwenck J, Sonanini D, Cotton J M, Rammensee H G, la Fougère C, Zender L and Pichler B J 2023 Advances in PET imaging of cancer *Nat. Rev. Cancer* **23** 474–90
- Van Sluis J, De Jong J, Schaar J, Noordzij W, Van Snick P, Dierckx R, Borra R, Willemsen A and Boellaard R 2019 Performance characteristics of the digital biograph vision PET/CT system *J. Nucl. Med.* **60** 1031–6

- Smith C L C, Yaqub M, Wellenberg R H H, Knip J J, Boellaard R and Zwezerijnen G J C 2024 Ultra-low foetal radiation exposure in 18F-FDG PET/CT imaging with a long axial field-of-view PET/CT system *EJNMMI Phys.* **11**
- Smith R, Capotosti F, Schain M, Ohlsson T, Vokali E, Molette J, Touilloux T, Hliva V, Dimitrakopoulos I K, Puschmann A, Jögi J, Svenningsson P, Andréasson M, Sandiego C, Russell D S, Miranda-Azpiazu P, Halldin C, Stomrud E, Hall S, Bratteby K, Tampio L'Estrade E, Luthi-Carter R, Pfeifer A, Kosco-Vilbois M, Streffer J and Hansson O 2023 The α -synuclein PET tracer [18F] ACI-12589 distinguishes multiple system atrophy from other neurodegenerative diseases *Nat. Commun.* **14**